Timescale and spatial distribution of local plastic events in a two-dimensional microfluidic crystal

Ya Gai, Alison Bick, and Sindy K. Y. Tang

Phys. Rev. Fluids **4**, 014201 — Published 8 January 2019

DOI: 10.1103/PhysRevFluids.4.014201

Timescale and spatial distribution of local plastic events in a two-dimensional microfluidic crystal

Ya Gai, Alison Bick, and Sindy K.Y. Tang

Department of Mechanical Engineering, Stanford University, Stanford, CA 94305, USA

*sindy@stanford.edu

Abstract

When a microfluidic crystal consisting of a concentrated emulsion flows in a convergent channel, the boundary conditions enforce a sequence of droplet rearrangements, also known as T1 events. At low flow rates, these T1 events are shown to be periodic both in space and in time, giving rise to a surprisingly ordered flow pattern. At high flow rates, however, the order is lost. To understand the transition from order to disorder, this paper examines the timescale and the spatial distribution of T1 events during the flow of a monolayer of monodisperse droplets within a concentrated emulsion confined in a convergent tapered microchannel. We show that the duration of a single T1 event consists of three distinct regimes with two transitions upon an increase in the applied flow rate. The first transition can be understood as a change in the forces that dominate during the T1 event, and the second transition can be associated with the emulsion transitioning from a solid-like state to a liquid-like state. Our results suggest that the loss of order in the flow of the concentrated emulsion, or the microfluidic crystal, is directly associated with the solid-like to liquid-like transition of the emulsion. Practically, our results are significant in understanding the relationship between the macroscopic property and the microscopic flow structures of the emulsion, as well as in guiding the design of flow control elements in microfluidic devices.

1 Introduction

The transition between order and disorder has been of long-standing interest in physics and engineering [1], and is essential to many aspects of science in understanding the emergence of complex phenomena from oscillators to swarming behaviors in animals [2,3]. Two-phase microfluidic flows have provided a simple experimental platform to study such phenomena, where hydrodynamic interactions have given rise to collective dynamics and order [4-8]. Most prior works have focused on emulsions or foams in the dilute regime. By studying an emulsion in the concentrated regime, we have recently identified a new type of order in the flow of a concentrated emulsion in a tapered microfluidic channel [9]. The concentrated emulsion consists of a monolayer of monodisperse water-in-oil drops with a volume fraction of $\varphi \sim 85\%$. We found that the velocity profiles of individual drops in the emulsion show periodic patterns in both space and time. We showed that this order can be explained by treating the system as a soft crystal in an extrusion flow, which causes the reorganization of the internal structure of the crystal in a highly ordered manner. Nevertheless, the conditions at which this order transitions to disorder remain unclear. The goal of this paper is to examine the characteristics of the elementary topological events—T1 events—that underlie the reorganization of the internal structure of the crystal. In particular, we focus on the effect of the applied flow rates on the temporal and spatial distribution of the T1 events, and the conditions that determine the transition from ordered to disordered flows in the microfluidic crystal.

From a more practical perspective, the flow of emulsions underlies many industrial processes ranging from oil recovery, polymer manufacturing, to food

processing [10-12]. Recent advances in high-throughput droplet microfluidic applications also relies on the flow of emulsions, where individual droplets act as separate biochemical reactors [13,14]. Here, the ability to manipulate drops in the form of a concentrated emulsion—an emulsion with a high disperse-phase volume fraction of $\varphi > 80\%$—is important to ensure uniformities in the flow profile and the associated incubation duration of the drops [15-17]. As the number of drops used increases for applications such as the directed evolution of enzyme where a large library of mutants ($>10^7$) is screened [14,18], the ability to process drops in a concentrated manner becomes increasingly critical as it removes the need to handle large volumes of the continuous phase for the same number of drops, and can lead to a reduction in the cost and time in processing these drops [19-22].

The bulk mechanical behavior of concentrated emulsions has been relatively well characterized. Above the random close packing limit (φ_{RCP} ~64%), droplets in an emulsion form a fragile network that has a macroscopic viscoelastic response [23,24]. Under a small load, drops remain trapped in a metastable configuration, and the emulsion behaves like an elastic material. When the applied stress increases beyond the emulsion's yield stress, a series of structural changes occurs, and the emulsion starts to flow. In the absence of coalescence, such structural changes have been shown to be dominated by a collection of local droplet rearrangements, also known as T1 events [25-27]. A T1 event is an elementary topological event that involves the exchange of neighbors between two adjacent pairs of drops. This topological event consists of one pair of diverging drops (highlighted by red circles in Figure 1a) and one pair of converging drops (highlighted by green circles in Figure 1a). At the beginning of a T1 event, the two drops in red circles

are adjacent separating the two drops in green circles. After an intermediate unsteady configuration, the two drops in green circles become neighbors, separating the two drops in red circles at the end of the T1 event.

Previous studies on T1 events focused mainly on establishing the connection between the frequency of T1 events and the fluctuations in macroscopic stresses or energy. These studies have demonstrated that T1 events affect the bulk rheology of the material by relaxing macroscopic stresses [25,26,28,29]. The timescale that describes individual T1 events is less explored but is important for understanding the flow of emulsions. Fundamentally, the duration of a T1 event is set by a balance between the driving force and the dissipative force. If we consider a system with a length scale of the four drops participating in a T1 event only, the driving force arises from repulsive inter-droplet interactions, which is a function of surface tension, as the distance between the droplet centers becomes less than their diameter. Depending on the system, the dissipative force is determined by the detailed mechanism of dissipation that can be contributed by bulk viscosities, or interfacial viscosities, or both.

In a slowly-driven dry foam, the duration of a T1 event was shown to be determined mainly by the interplay between surface tension and the interfacial viscous modulus [30,31]. For wet foams and granular media, this duration depends mainly on the ratio between the osmotic pressure representing the contact force among unit particles arising from dense packing, and the bulk fluid viscosity [32-34]. A common assumption in these studies is that applied rates are sufficiently low so that the system remains close to a quasi-static limit. In many practical applications, however, the emulsion is driven at high flow rates where the quasi-static limit assumption does not apply. It is thus

important to understand the dependence of T1 timescale on flow rates beyond the quasi-static limit.

With respect to the spatial distribution of T1 events, previous works on foams, emulsions, and granular materials revealed that the location of T1 events was correlated to the localization of stress field, where the local stress first built up and then became released through the T1 events [26,29,35,36]. Furthermore, at sufficiently low strain rates, several studies on foams indicated that successive T1 events were not randomly distributed in space but rather localized [37]. Similar observations were also reported in our recent work, in which we slowly drove a concentrated emulsion in a slightly tapered microchannel and the T1s occurred only in well-defined spatial locations [9]. However, it is unclear how the localization of T1 events would change as the strain rate increases.

In this work, we study the timescale and the spatial distribution of T1 events experimentally during the flow of a monolayer of monodisperse droplets within a concentrated emulsion ($\varphi \sim 85\%$) confined in a convergent tapered microchannel. Due to the converging channel width, droplets rearrange through a series of T1 events as they flow from the wide end of the channel towards the narrow end. Such geometry has been shown to induce T1 events in foams and emulsions [9,26,38]. Practically, the tapered geometry is commonly used in many high-throughput, droplet-based serial interrogation processes. Understanding the temporal and spatial distribution of T1 events in such geometry can thus facilitate the design of on-chip flow control devices [9,13,20,21]. Here we examine the effect of flow rates on the duration of a single T1 event, the frequency of occurrence of T1s, and the spatial distribution of T1s. We show that the duration of a single T1 event consists of three distinct regimes with two transitions when the applied

flow rate increases. The first transition can be understood as a change in the forces that dominate during the T1 event. The second transition can be associated with the emulsion transitioning from a solid-like state to a liquid-like state, which is manifested in changes in the time-averaged drop velocity profiles. Finally, we conclude that the loss of order in the flow of the concentrated emulsion, i.e., the microfluidic crystal, is directly associated with the solid-like to liquid-like transition of the emulsion. Our current work has focused on presenting the timescale and the spatial distribution of T1 events from an experimental perspective, and applying simplified scaling analysis to interpret our results. We have further identified opportunities for detailed theoretical analysis and modeling in future investigations.

2 Methods

2.1 Device fabrication and droplet generation

We used methods in soft lithography to fabricate microchannels in poly(dimethylsiloxane) (PDMS) [39]. We generated monodisperse 50-pL droplets using flow-focusing nozzles [40]. The volume dispersity of generated drops was less than 3%. The disperse phase was deionized water, and the continuous phase was a hydrofluoroether HFE-7500 (3M, St. Paul, MN). The viscosity of HFE-7500 was approximately 1.24 cP at 20°C, the temperature at which all experiments were performed. The continuous phase contained an ammonium salt of Krytox (2% w/w) as surfactant to stabilize the drops against coalescence. We used the Rame-Hart 290 contact angle goniometer (Rame-hart Co., NJ, USA) to measure the surface tension between the two phases. The surface tension was measured to be 26.25 mN/m. We collected the drops generated from the flow-focusing nozzles in syringes (Normject 1 mL). As water has a lower density than HFE-7500 does (ρ = 1.63 g/mL), the drops creamed to the top of the syringes to form an emulsion with volume fraction $\varphi \sim 85\%$ after 6 hours of storage at room temperature. The size of the drops remained unchanged after this storage time. The microchannels were rendered hydrophobic by treatment with Aquapel (Pittsburgh, PA) to avoid droplet wetting of the wall.

2.2 Emulsion injection and image recording

Figure 1b shows a microscopic image of the microchannel into which the concentrated emulsion was injected. For all our experiments, the probed channel region was the same as that shown in Figure 1b. The blue dots highlight the approximate

locations of T1 events (see section 2.3 for the method to identify T1 events). The channel was tapered with a linearly decreasing width leading to a constriction downstream having a width of 30 μm. The half-angle of the taper was 5°. For all experiments, the width of the channel W was a function of x position only, and the channel height H was fixed at H=30 μm. At this height, the drops flowed as a monolayer as their diameter D when spherical was D=46 μm. To drive the flow of the emulsion, we used a syringe pump to apply a constant volumetric flow rate (NewEra). To vary the capillary numbers, we either changed the applied flow rates, or recorded T1 events in control volumes at different x locations (see sections 2.5 and 2.6). For each experiment, the applied flow rates and the corresponding capillary number of each control volume were given in Supplementary Material Table S1 [41]. We used an inverted optical microscope combined with a high-speed camera (Phantom v7.3, Vision Research) to record videos of emulsion droplets flowing in the microchannel. We used customized *MATLAB* scripts to track all droplets in each frame and constructed Voronoi tessellation to identify T1 event.

2.3 Method to identify T1

Voronoi tessellation is a mathematical framework that defines the local structure of a set of discretized points in space. Previous simulations and experiments have shown that Voronoi tessellation is an efficient tool in the studies of particle systems and related hydrodynamics, especially in problems involving the topological changes of the particle structure [42-44]. More specifically, Voronoi tessellation works by partitioning the space into a collection of polygons (known as Voronoi cells) based on the particle centroid so that each polygon contains only one particle in its center. In our case, the Voronoi cells

are defined based on the centroid locations of droplets within the field of view. Each edge of a Voronoi cell is shared by two neighbor droplets. Therefore, the number of edges of a Voronoi cell indicates the total number of neighbors of the corresponding droplet.

After constructing the Voronoi cells for all droplets in each frame, we followed a two-step procedure to identify a T1 event. First, we searched for drops that have 5 neighbor drops. At a volume fraction of $\varphi \sim 85\%$, the drops were typically hexagonally-packed in their static configuration, and each drop had 6 neighbors. During a T1 rearrangement, however, one participating drop (highlighted in blue in Figures 2a and 2b) would be surrounded by 5 neighbors. Equivalently, the search for a 5-edged Voronoi cell became a necessary condition for a T1. Second, the 5-edged cell must have an edge that expanded in time, which we refer to as a growing edge. This growing edge corresponded to an artificial "film" created by the approaching pair of drops (see the Voronoi edge highlighted in red in Figures 2a and 2b). The concept is similar to a T1 event in a dry foam system, which involves the creation of a new film by the evolution from a single four-fold to two three-fold film junctions [30,31,45]. Different from a dry foam system, however, the physical "film" in our emulsion system at a disperse phase volume fraction of $\varphi \sim 85\%$ had a finite thickness and a different flow profile within the film. Nevertheless, the growing edge in our emulsion is directly analogous to the film created by a T1 event in the dry foam system. The requirement of the presence of a growing edge, together with a 5-edge cell, completes the definition of a T1. If the above two requirements were met, a T1 event in the emulsion was identified. The onset time of the T1 event t_{T1} was defined as the moment when the growing edge started to increase

($t_{T1} = t_{l\prime=0}$, see Figure 2). The location of the T1 event was approximated by the center of the corresponding 5-edge cell at t_{T1}.

2.4 Measured quantities

Before we present the results, we briefly discuss the measured quantities in our study.

Duration of a single T1 event (T). We extracted T by monitoring the temporal evolution of the length of the growing edge $l(t)$. Figures 2a and 2b show the Voronoi tessellation for two T1 events. We observed that the growing Voronoi cell edges (highlighted red segments) evolved at different timescales. The growing edge at $Ca = 2.1 * 10^{-3}$ evolved at a timescale that was 3 order of magnitude shorter than that at $Ca = 4.9 * 10^{-7}$ (see section 2.5 for the definition of capillary number Ca). This observation suggested the duration of the T1 event was rate-dependent. Figures 2c-2d plot representative $l(t)$ for various T1 events at different Ca. We normalized the growing edge length as $l'(t) = \frac{l(t)}{l_{max}}$, where $l(t)$ is the instantaneous growing edge length, and l_{max} is the maximum length of the growing edge during a measurement. We defined T to be the time required for l' to reach $l'(t = T) = 0.90$.

Scaled T1 event count (P_{T1}). We defined the scaled T1 event count P_{T1} as the number of T1 events per drop advected through a control volume CV (see section 2.6 for details). We measured the time Δt required for the total number of drops $N_{drop} \geq 2000$ to advect through a given CV at a given flow rate. Within this CV, we counted the total number of T1 events N_{T1} that occurred during Δt. We defined N_{cv} to be the number of drops whose peripheries were completely enclosed by this CV when there was no flow. The definition of the scaled event count is given in Eq. (1).

$$P_{T1} = {N_{T1}}/{N_{drop}} \qquad (1)$$

The time between two successive T1 events ($\boldsymbol{dT}$). *dT* was defined to be the time interval between the onset time t_{T1} of two successive T1 events.

Drop velocities during a T1 event ($\boldsymbol{U}$). We tracked the centroid displacement of each drop. Drop velocity was calculated as the centroid displacement divided by the time interval over which the drop centroid moved about one drop diameter. We defined *U* to be the centroid velocity of the drop corresponding to the 5-edge Voronoi cell in the T1 event.

2.5 Non-dimensionalization

There are three primary timescales in our system. (1) Single droplet relaxation time $T_{drop} = \frac{\mu R}{\sigma}$, where μ is continuous phase viscosity, *R* is droplet radius assuming a spherical shape, and σ is surface tension. This timescale is associated with the deformation of a single drop, which is controlled by the competition between viscous stress and surface tension [46]. (2) The duration of a single T1 event T. (3) The time interval between two successive events dT.

In the rest of the paper, we present our results using the following dimensionless parameters in Eq. (2).

$$T' = \frac{T}{{\mu R}/{\sigma}},\ dT' = \frac{dT}{{\mu R}/{\sigma}},\ Ca = \frac{\mu U}{\sigma} \qquad (2)$$

where we choose droplet relaxation time $T_{drop} = \frac{\mu R}{\sigma}$ to non-dimensionalize *T* and *dT*. The dimensionless drop velocity of a T1 event becomes the capillary number *Ca* in this case.

2.6 Definition of control volume (CV)

We segmented the probed channel region into 6 control volumes (CV) for all our experiments and grouped the results as a function of *Ca*. These CVs are highlighted in Figure 1c. Each CV had a width (measured along *x*-direction) equal to 5*D*, where *D* is one droplet diameter. For all applied flow rates *Q* and CVs, the maximum variation in *U,* and hence *Ca,* was below 30%, and the maximum variation in *T'* was below 38%. Within one CV at a given flow rate *Q*, we conducted a batch of *T'* measurements with >200 T1 events. We defined $\langle T' \rangle$ and $\langle Ca \rangle$ to be the value of *T'* and *Ca* averaged over >200 measurements, respectively. The locations of CVs were chosen to cover the rearrangement zones. As we will describe in more details in section 3.3, the rearrangement zones were the locations where the number of row of drops reduced by one and were also the locations where all T1 events occurred at low flow rates. Our choice of CVs covered all T1 events in Regime 1 and Regime 2 until the flow rate increased to Regime 3, where T1 events were no longer localized within the rearrangement zones. T1 events that occurred outside the CVs were ignored (see sections 3.3 for details).

3 Results

3.1 Duration of a single T1 event

Figure 3a plots representative distributions of T' at 5 different values of $\langle Ca \rangle$. We observe that the distribution of T1 duration was broad. The overall shape of the distribution was consistent with previous studies in a wet foam system [45]. While the investigation of such distribution is out of the scope of our current study, previous works have shown that the shape of the distribution can be attributed to the relaxation modes of the system, the contact number, and fluctuation in rearrangement event size [47,48]. Important to our study here, the variation in $\langle Ca \rangle$ did not change the distribution. Therefore, using the averaged value $\langle T' \rangle$ to describe the duration of the individual T1 event should be robust within the range of our study. We will thus be using $\langle T' \rangle$ as the event duration for the rest of the paper.

Figure 3b shows T' as a function of Ca. The results of $\langle T' \rangle$ can be grouped into three distinct regimes. We refer to them as Regime 1, Regime 2, and Regime 3, respectively. In Regime 1 ($10^{-7} < Ca < 10^{-6}$), $\langle T' \rangle$ was not sensitive to the variation in $\langle Ca \rangle$. The scaling followed $\langle T' \rangle \sim \langle Ca \rangle^{-0.14}$. In Regime 2 ($10^{-6} < Ca < 10^{-3}$), $\langle T' \rangle$ decreased with $\langle Ca \rangle$. The scaling followed $\langle T' \rangle \sim \langle Ca \rangle^{-0.61}$. In Regime 3 ($10^{-3} < Ca < 10^{-2}$), $\langle T' \rangle$ decreased with $\langle Ca \rangle$. The scaling followed $\langle T' \rangle \sim \langle Ca \rangle^{-0.37}$. The distinct regimes are also reflected in the representative profiles of $l'(t)$ in Figures 2c-2e. In Regime 1, all profiles of $l'(t)$ collapsed approximately into one curve. In Regime 2 and Regime 3, the profiles of $l'(t)$ no longer collapsed into a single curve.

3.2 Frequency of occurrence of T1 events

Figure 4a shows the number of T1 events per drop advected through a CV, P_{T1}, as a function of Ca. A large value of P_{T1} corresponds to a high T1 frequency, and vice versa. P_{T1} consisted of three regimes, and the transition between each regime occurred at similar Ca values as those in *T'* (Figure 3b). In Regime 1, P_{T1} remained relatively insensitive to *Ca*. In Regime 2, there was a slight increase in P_{T1} with increasing *Ca*. In Regime 3, there was a sharp increase in P_{T1} with increasing *Ca*.

As another way to present the frequency of occurrence of T1 events, Figure 4b plots *dT'*, the difference in the onset time of two successive T1 events, as a function of Ca. Representative distributions of the onset time of T1 are shown in Figures 4c to 4e. The results of *dT'* cover Regime 1 and Regime 2 ($10^{-7} < Ca < 10^{-3}$) only. In Regime 3, we observed that multiple T1 events often occurred simultaneously at all values of *Ca* (see Figures 4e). Thus, the definition of *dT'* does not apply in Regime 3 and was not plotted in Figure 4b. Within the range of Ca shown in this plot, *dT'* decreased with increasing Ca. The scaling followed $dT' \sim \langle Ca \rangle^{-0.86}$. The scaling of *dT'* is in line with Gopal and Durian's work, which reported a linearly decreasing time between two successive events with increasing strain rate [49]. We also note that there was no clear boundary observed between Regime 1 and Regime 2.

Comparing *T'* and *dT'*, we found that in Regime 1 and Regime 2, *dT'* was at least a few times larger than *T'*, suggesting that T1 events in both regimes were intermittent. At the crossover between Regime 2 and Regime 3 ($Ca \sim 10^{-3}$), *dT'* became close to *T'*, suggesting T1 events were no longer intermittent beyond $Ca \sim 10^{-3}$.

3.3 Spatial distribution of the T1 events

Figures 5a-5c plot heatmaps showing the spatial distributions of all T1 event locations by tracking a total of 2000 drops have advected through. A major observation is that T1 events occurred in relatively fixed spatial locations in Regime 1 and Regime 2, while they occurred throughout the whole probed channel region in Regime 3.

In Figures 5a and 5b (Regime 1 and Regime 2), the T1 events occurred in spatial locations that were identified in our previous work as "rearrangement zones" (also see Figures 6a and 6b), where a cascade of successive T1 events occurred and the number of rows of drops reduced by one due to a tapered channel geometry at low *Ca* values [9]. As our drops are monodisperse, our emulsion is analogous to a crystal, and a T1 rearrangement is analogous to a crystal dislocation. The cascade of the successive T1 events in the rearrangement zone can be modelled as the gliding motion of crystal dislocations on its slip plane. These rearrangement zones can be predicted by the Read-Shockley model of low-angle grain boundary [9]. For the probed channel region, the width of each rearrangement zone was within 4 droplet diameters, and the separation of two rearrangement zone was about 5 droplet diameters. Between two rearrangement zones, no T1 event was observed (see our previous work [9] for details). Within the rearrangement zones, the T1 events appeared less localized in Regime 1 than they did in Regime 2. This is likely a result of the bulk flow fluctuation induced by the pulsation of the syringe pump motor at the low applied flow rates in Regime 1. In Figure 5c (Regime 3), the T1 events were no longer localized to the rearrangement zones and were instead spread throughout the entire channel.

3.4 Flow features in different regimes

In this section, we present the flow profiles in different T1 regimes. We focus on three flow features of the emulsions: the trajectories of droplets, the time-averaged droplet velocity profiles, and the orientation of the propagation of successive T1 events. The first two features are especially important for practical applications in droplet microfluidics for the design of effective flow control and on-chip droplet manipulations [15,16]. Figures 6a-6c plot the trajectories of droplets driven at different flow rates in the tapered microchannel. Each plot was generated by tracking a total number of 2000 of drops advected through the channel. The position of each marker represents a droplet centroid at a given time. These markers overlap and appear as continuous lines, representing the trajectories of all droplets. The inset shows the time-averaged droplet velocity profile at a given x location.

In Figures 6a and 6b (Regime 1 and Regime 2), droplets participated in T1 events inside rearrangement zones only, where the number of rows of drops reduced by one. The trajectories of all droplets were highly repeatable. The time-averaged velocity profiles of the drops at a given x position were plug−like. At the given Ca range, the plug-like velocity profiles at a given x position are consistent with previous reports on concentrated emulsion flowing in confined channel with a constant width [15]. In Figure 6c (Regime 3), no rearrangement zones were observed. Instead, the droplet trajectories appeared more irregular than those shown in Figures 6a and 6b. The time-averaged droplet velocity profiles at a given x position also became more parabolic than those in Regime 1 and Regime 2. Such velocity profile indicates that the bulk emulsion started to flow laminarly.

To further investigate the droplet dynamics in the three regimes, we examined the droplets involved in the T1 events. A close examination of the flow revealed that successive T1 events only occurred and propagated along the 60° direction relative to the *x*-axis in Regime 1 and Regime 2 (Figures 6d and 6e), while they occurred along both the 60° and ~0° directions (i.e., the direction of the imposed flow) relative to the *x*-axis in Regime 3 (Figure 6f). In addition, in Figure 6f, we observe two T1 events (red-green pair and yellow-purple pair) that occurred simultaneously within one snapshot.

4 Discussions

Our results on T1 duration and frequency indicates three distinct regimes separated by two transitions at $Ca_{1-2}\sim10^{-6}$ and $Ca_{2-3}\sim10^{-3}$, respectively. The subscript denotes the corresponding regimes where the transition occurs. In the following, we show that the first transition at Ca_{1-2} is associated with the increased effect of the frictional forces between the drops and between the drops and the wall as *Ca* increased beyond Ca_{1-2}, and the second transition at Ca_{2-3} is associated with the emulsion transitioning from a solid-like state to a liquid-like state.

4.1 Transition between Regime 1 and 2: scaling analysis

We consider the scaling analysis of a simplified force model that describes the motion of the drops during a T1 event. For a two-dimensional concentrated emulsion confined in a microchannel, there are two major types of forces acting on a drop i: a repulsive force F_r arising from droplet "contacts", and frictional forces F_f arising from the relative motion between the drops and the channel wall as well as that between the drops [50]. In our system, the drops were deformed and separated by a thin film of continuous phase, and the "contact" can be characterized by the difference in the distance between two droplet centroids and the droplet diameter when undeformed (see Supplementary Material Note S2 for details [41]). The equation of motion for drop *i* can be expressed as:

$$(U_i - U_i^{\infty}) = \frac{f(\varphi)}{6\pi\mu R} * (F_r + F_f) \qquad (3)$$

where U_i is the instantaneous velocity, U_i^{∞} is the averaged velocity field due to the applied flow rates, and $f(\varphi)$ is a correction factor that accounts for the reduced drop mobility at a high volume fraction [28,50].

During a T1 event, we estimate that the drop moves a typical distance of *R* on a timescale equal to *T*, thus $(U_i - U_i^{\infty}) \sim \frac{R}{T}$. We model the repulsive force F_r by the modified Hertz theory for compressed micro-elastomeric spheres with large deformation, which should also apply to the deformed drops due to the dense packing in our system. Previous studies by Liu et al. and Seth et al. have suggested the scaling of F_r follows $F_r \sim \sigma R b \varepsilon^c$, where *b* and *c* are fitted parameters that depend on the degree of compression, and ε is the compression strain [50,51]. For the frictional force F_f, prior studies on the emulsion and foam system have suggested that both the wall frictional force as well as the viscous dissipation force follow the scaling $F_f \sim \sigma R C a^n$, where the value of *n* depends strongly on the mobility of the interface (see Supplementary Material Note S2 for details) [41,52-56].

In Regime 1, due to the small *Ca,* we estimate that F_f is at least a few orders of magnitude smaller than F_r (see Supplementary Material Note S2 [41]). We thus hypothesize F_f was negligible in determining *T* in Regime 1. Ignoring F_f and substituting $F_r \sim \sigma R b \varepsilon^c$ and $(U_i - U_i^{\infty}) \sim \frac{R}{T}$ in Eq. (3), we obtained a scaling of T' as shown in Eq. (4).

$$T' \sim \frac{10}{f(\varphi) b \varepsilon^c} \qquad (4)$$

At a volume fraction of $\varphi \sim 85\%$, previous work on soft particle flows reported $f(\varphi) \sim 0.01$, $\varepsilon \sim 0.1$, $b = 32$, and $c = 3$ (see Supplementary Material Note S2)

[41,50,51]. Using these values, Eq. (4) predicts $T' \sim 10^4 - 10^5$, which is on the same order of magnitude as the lower end of the error bar in our results in Regime 1 ($T' \sim 10^5$).

In Regime 2, as *Ca* increases, F_f also increases and becomes comparable with F_r. Following our scaling argument, we obtain the scaling $T' \sim Ca^{-n}$ from Eq (3). Previous studies on quasi-two-dimensional foams and emulsions reported the value of *n* to be between 0.5 and 2/3 [52,53,57]. The variation in the reported *n* value could be caused by the difference in the detailed interfacial dynamics [52,57]. Our results in Regime 2 (Figure 3b) show $T' \sim Ca^{-0.61}$, which lies in the range of the prediction. In our system, the actual interface was likely partially mobile, which could possibly explain why our results in Regime 2 lie between the scaling of $Ca^{-0.5}$ and $Ca^{-2/3}$. In Regime 3, our results show a dependence of $T' \sim Ca^{-0.37}$, which deviates from the prediction of the scaling analysis. We rationalize this deviation as follows. At high *Ca* values, the drop contact facets are rapidly squeezed, leading to a strong film drainage effect. As a result, the simplified force model that applies to Regimes 1 and 2 may no longer apply in this regime. To explain the scaling in this regime (i.e., the exponent of -0.37) will likely require a non-equilibrium, time-dependent model which is out of the scope of the current work. In addition, we observe that the T1 duration is almost identical to the time interval between two consecutive T1 events at the crossover *Ca* between Regime 2 and Regime 3 (see Figure 4b). This suggests that the drops in a single T1 event do not have sufficient time to relax or complete the initial T1 before the next T1 event starts. In other words, in Regime 3, the T1s are likely coupled and no longer isolated from each other like those in Regimes 1 and 2. To further understand the dynamics in Regime 3, we proceed to examine the frequency

of occurrence and the spatial distribution of T1 events as well as the flow profiles in the next sections.

4.2 Transition from Regime 2 to Regime 3: solid-like to liquid-like transition

In general, both the duration of a single T1 event and the frequency of T1 events are known to play important roles to relax the imposed stress during the emulsion flow [28,49,58]. As the flow transitions from Regimes 1 and 2 to Regime 3, the drops participate in an increasing number of T1s both temporally and spatially (Figures 4-5). More specifically, inside the CVs, the T1 event count P_{T1} in Regime 3 increases dramatically in comparison with that in Regime 1 and Regime 2 (Figure 4a). Outside the CVs, T1 events occur between two rearrangement zones in Regime 3, while they occur only within the rearrangement zones in Regime 1 and Regime 2 (Figure 5). Therefore, in Regime 3, while the fast flow does not allow the drops involved in a T1 to complete the process and relax, additional number of T1 events are nucleated to relax the imposed stress. This observation is consistent with previous studies on foams and emulsions, where an increased frequency of rearrangements is correlated to a faster stress relaxation during the flow [25,28,49].

Upon the transition from Regime 2 to Regime 3, the emulsion flow exhibits a critical change in the velocity profile that characterizes a solid-like to liquid-like transition. Below Ca_{2-3}, the time-averaged droplet velocity profiles are plug-like (Figures 6a and 6b). These plug-like velocity profiles resemble those described in previous studies, in which emulsions display solid-body motion with zero velocity gradient transverse to the shear direction when the applied strain rate is low [59,60]. This solid-body motion with a plug-like velocity profile arises from the wall slip effect on the surface of a plate, a cones, or a cylinder of a rheometers, and is considered characteristic of a solid material [60,61]. Above Ca_{2-3}, the droplet velocity profiles become

increasingly parabolic (Figure 6c). These parabolic velocity profiles are characteristic of channel flow of a viscous liquid. The change in flow profile from plug-like to parabolic thus indicates that the transition from Regime 2 to Regime 3 corresponds to a solid-like to liquid-like transition and reflects the nature of the concentrated emulsion as a viscoelastic material.

Accompanied with the transition from Regime 2 to Regime 3, the droplet trajectories, the spatial distribution of T1 events, and the orientation of successive T1 events also become increasingly different. In Regimes 1 and 2, we observe highly regular and repeatable droplet trajectories and the drops rearrange within the rearrangement zones only. The solid-like behavior is evidenced by the fact that successive T1s occurred along directions that are 60° relative to the *x*-axis only (Figures 6d and 6e). As detailed in our prior study, the motion of the T1s can be explained purely from a solid mechanics point of view by considering the emulsion as a two-dimensional hexagonally-packed crystal and the T1 as a dislocation. The T1 dislocations are present due to the boundary conditions of the tapered wall which imposes a geometrically necessary dislocation array to accommodate the mis-orientation of the crystal in the taper [9]. The Burgers vector of the dislocation is at 60° from the *x*-axis [62]. The T1 dislocation can glide on its slip plane, which contains the Burgers vector. The gliding motion is driven by the resolved shear stress on the slip plane, where the compressive stress in the *y* direction is greater than that in the *x* direction. In Regime 3, in contrast, the droplet trajectories are spread out in the whole probed channel region without following any specific pattern. The flow proceeds through T1 events that are continuously occurring which are no longer localized in the rearrangement zones. T1 events occurred along the direction of the imposed flow

in addition to the 60° direction (Figure 6f). The T1 events along the imposed flow direction are induced by an increased frictional stress from the channel wall and an increased viscous effect among the drops, which lead to a more liquid-like behavior at high *Ca* [9,49].

To further support that the transition from Regime 2 to Regime 3 represents a solid-like to liquid-like transition, we examine the Deborah number. The Deborah number $De = \frac{T_r}{R/U}$ can be used to distinguish the solid-like and the liquid-like regime, where T_r is the relaxation timescale of the flow, and R/U represents the timescale associated with the droplet advection. In terms of dimensionless quantities, $De = T_r' * Ca$, where T_r' is the dimensionless relaxation timescale. If $De \ll 1$, the drops have sufficient time to complete the full relaxation process during the droplet advection, and the material is solid-like. On the other hand, if $De \gg 1$, the drops cannot fully relax before they participate in next rearrangement, and the material is liquid-like. The crossover between the two regimes can be obtained by setting $De = 1$. The choice of T_r is not straightforward, however. Several studies have suggested that a single relaxation timescale is insufficient to describe the flow of foam, emulsion, and particle suspension [11,49,63]. Here, we choose to use different T_r in different regimes for the following reasons. In Regime 1 and Regime 2, the emulsion flow is dictated by intermittent and localized T1 events. The duration of each event *T'* is at least several times lower than the time interval between two successive events *dT'*, suggesting that the latter is the rate-limiting factor in determining the macroscopic stress relaxation of the system. Therefore, we set the timescale associated with the emulsion flow to be $T_r' = dT'$ in these two regimes. In Regime 3, the flow is accompanied by multiple simultaneous T1 events

within one event duration. The rate-limiting factor is thus the event duration. In this regime, $T_r' = T'$.

Following the choice of T_r in our system, we summarize our results of event duration *T'*, time between events *dT'*, inverse of capillary number $1/Ca$, and Deborah number *De* in one plot in Figure 7. Based our results, setting $De = 1$ gives a $Ca_{S-L} \sim 2 * 10^{-3}$. The value of Ca_{S-L} is very close to the transition between Regime 2 and Regime 3 at $Ca_{2-3} \sim 10^{-3}$. Therefore, we can conclude the transition from Regime 2 to Regime 3 corresponds to a transition of the emulsion from a solid-like state to a liquid-like state. As an additional note, the major difference between Regime 1 and Regime 2 lies in the single T1 event duration *T'*: in Regime 1, *T'* is insensitive to *Ca*; in Regime 2, *T'* decreases with *Ca*. However, *T'* in these two regimes is not the rate-limiting factor and does not enter the calculation of *De*. This explains why the flow features (droplet trajectories and velocity profiles) are similar in Regime 1 and Regime 2.

Finally, we relate the above discussion to the order-to-disorder transition in the microfluidic crystal. Previously, we identified that the ordered flow patterns of microfluidic crystal was lost at $Ca \sim 10^{-2}$ measured at the constriction [9]. This value of *Ca* corresponds to the beginning of Regime 3 in the present study. Below this value, the emulsion was in Regimes 1 and 2 and was expected to be solid-like. The T1s were isolated and did not interact. Their propagation was analogous to a dislocation glide along crystal plane and the resulting flow profile was highly ordered. As the applied flow rate and the corresponding Ca increased above Ca_{2-3}, the emulsion transitioned to Regime 3 and was expected to become liquid-like. In this regime, successive T1 events occurred along the imposed flow direction. These T1s interacted with the T1s along the 60º slip

plane. Such interactions could then lead to various outcomes (e.g., the mutual blockage or annihilation of T1 dislocations), thereby disrupting the periodic slip dynamics and the ordered flow behavior. In other words, the loss of order in the flow of the microfluidic crystal as flow rate increases originates from the emulsion transitioning from a solid-like material to a liquid-like material.

4.3 Opportunities for future work

While the simplified scaling analysis helped explain our experimental results qualitatively, more comprehensive theoretical analysis and modeling is required to understand the results quantitatively. In this section, we briefly discuss the challenges and opportunities for further investigations.

At a microscopic level of a single droplet, the inter-drop repulsive force, the friction between drops in relative motion, and the friction between the drops and the channel wall must be examined in detail in our system. These forces depend strongly on parameters including drop interfacial property, applied strain rate, surface roughness of channel wall, and the degree of confinement [50,54,55,57,64]. The expression of these forces are expected to be non-trivial and can possess different forms depending on the details of the system. At the same time, care must be taken when summing the force contributions from neighboring drops and channel walls, which in turn depend on the dynamic packing of the drops (e.g., a drop with 5 neighbors versus a drop with 7 neighbors during a T1) and the location of the T1 event (e.g., a T1 away from channel side wall versus a T1 close to the side wall. The former consists of drops in contact with

top and bottom walls, while the latter consists of drops in contact with top, bottom and side walls).

At a macroscopic level of the bulk emulsion, precise prediction and measurement of the yield point is necessary to further validate our argument that the transition from Regime 2 to Regime 3, and hence the order-to-disorder transition in this microfluidic crystal, corresponds to a solid-to-liquid transition of the emulsion. While the rheology of bulk 3D emulsions has been studied extensively, those results are unlikely to be readily applicable to a 2D emulsion consisting of a monolayer of monodisperse drops. Several works have demonstrated differences in rheological properties, including constitutive equation, yield stress, and wall frictional stress, when the dimensionality of the emulsion reduces from 3D to 2D [54,61,65,66]. In addition, in our system, the use of the tapered wall as the boundary condition to impose the T1 dislocations is different from typical geometries (e.g., parallel plate, Couette cell, cone and plate) applied in previous studies in the rheometric flows of emulsions [45,58,61,65]. All these factors must be considered when matching the T1 transitions to the rheological properties of the probed 2D emulsion system. The investigation of these factors presents opportunities for future studies involving more advanced theoretical, computational and experimental work.

5 Conclusions

In summary, we have identified that the duration of a single T1 event consists of three regimes as a function of *Ca*, which was not reported before (see Table 1 for a summary). The transition from Regime 1 to Regime 2 at $Ca_{1\text{-}2}$ can be explained by a scaling analysis of a simplified force model. Two types of forces were considered in this model: a repulsive force due to the direct drop contact at high volume fraction, friction forces between the drops and between the drops and the wall. In Regime 1, *Ca* is small and friction forces are negligible. The motion of the drop is set mainly by the repulsive force, and is relatively insensitive to *Ca*. Thus, the scaling suggests that the T1 event duration is insensitive of *Ca,* consistent with our results. In Regime 2, friction becomes increasingly important. In this regime, our result shows $T' \sim Ca^{-0.61}$. Our result is consistent with the scaling analysis by using the friction of a quasi-two-dimensional foam or emulsion system.

The transition from Regime 2 to Regime 3 at $Ca_{2\text{-}3}$ is associated with the solid-liquid transition ($Ca_{2\text{-}3} \sim Ca_{S\text{-}L}$) of the emulsion. In Regimes 1 and 2 ($Ca < Ca_{2\text{-}3}$), the solid-like behavior is manifested in the plug-like time-averaged flow profiles. In these two regimes, the T1s occur along the 60º crystal slip planes only inside rearrangement zones, the droplet paths are repeatable. In Regime 3 ($Ca > Ca_{2\text{-}3}$), the liquid-like behavior is manifested in the parabolic time-averaged flow profiles. In this regime, the T1s are non-localized, and they occur along both 60º crystal slip planes and along the direction of flow. Droplet paths do not appear to follow any patterns.

Our results suggest that the loss of order in the flow of the concentrated emulsion, i.e., the microfluidic crystal, in a tapered geometry is directly associated with the solid-

like to liquid-like transition of the emulsion. Practically, our results are significant in understanding the relationship between the macroscopic properties and the microscopic behavior of the emulsion flow, as well as in guiding flow control methods in microfluidic devices. To gain a complete, quantitative understanding of the three T1 regimes, future work involving more advanced theories and computational schemes are required.

Acknowledgement

We acknowledge support from the National Science Foundation through the NSF CAREER Award No. 1454542.

Table 1. Summary of results

	Regime 1	***Regime 2***	***Regime 3***
Duration of a T1 event (T')	$T' \sim Ca^{-0.14}$	$T' \sim Ca^{-0.61}$	$T' \sim Ca^{-0.37}$
Scaled T1 event count (P_{T1})	Insensitive to *Ca*	Slight increase	Steep increase
Time between successive T1 events (dT')	*dT' > T'*, intermittent; T1s occur along 60º crystal slip planes only		*dT'≤ T'*, Continuous; multiple T1s occur simultaneously; T1s occur both along 60º crystal slip planes and along the direction of flow
Spatial distribution of T1	Localized in rearrangement zones		Non-localized
Flow features	Repeatable drop paths, plug-like time-averaged flow profiles		Irregular drop paths, more parabolic time-averaged flow profile

Figure 1. (a) Progression of a T1 event. The green circles highlight a converging pair of droplets. The red circles highlight a diverging pair. The time interval between two snapshots is 0.05 s. (b) Microscopic image of the emulsion flowing in the tapered microchannel. $x = 0$ is set as the left boundary of the field of view shown. The blue dot represents the center of the 5-edge Voronoi cell, which approximate the location of a T1 event. (c) Definition of control volume (CV). The blue markers (overlaid on top of each other) represent the locations of T1 events after 2000 drops advected through the field of view. Each red dashed box highlights a CV that has a width of 5 droplet diameters.

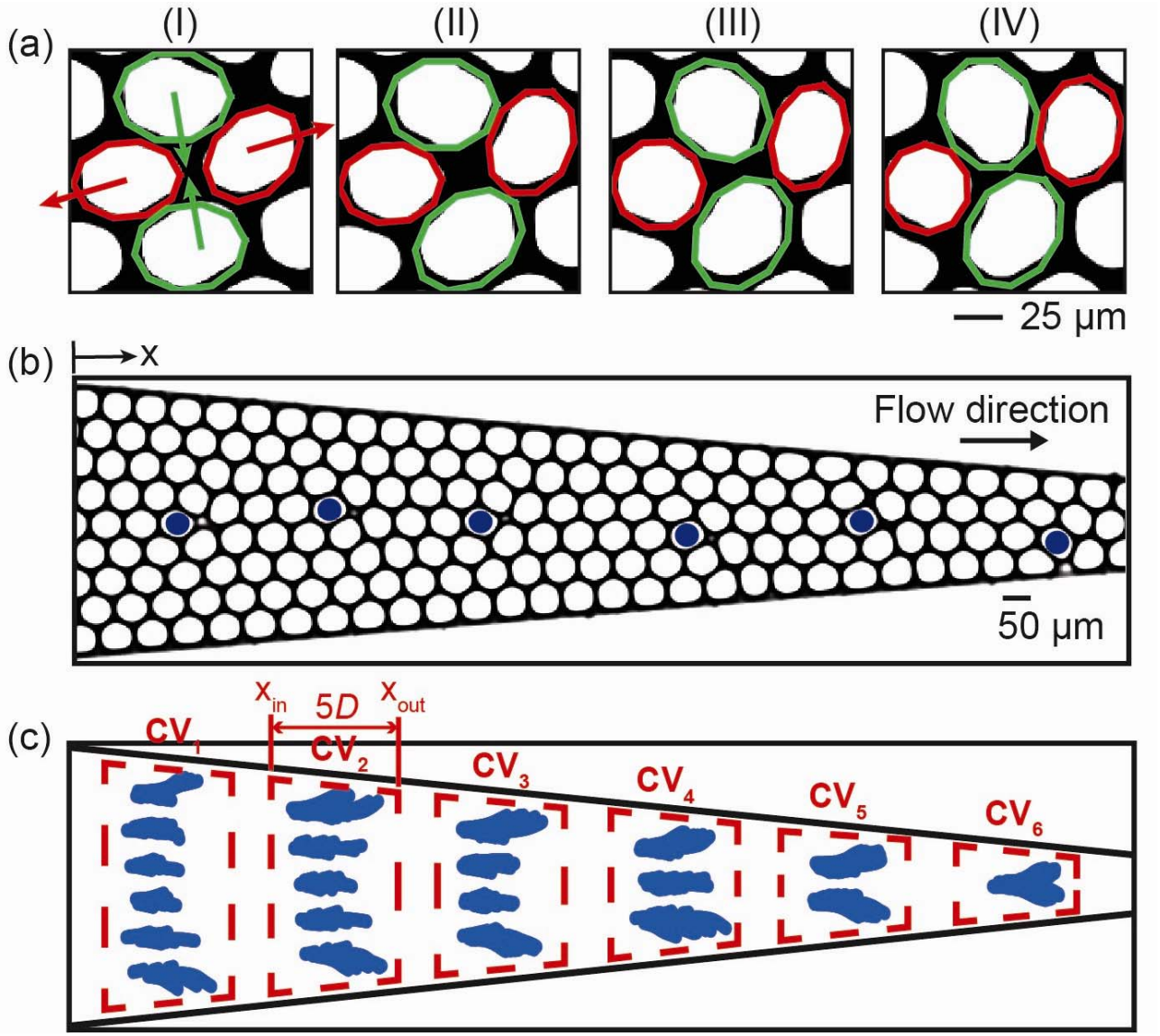

Figure 2. (a)-(b) Voronoi tessellation during a T1 event at (a) $Ca = 4.9 * 10^{-7}$ and (b) $Ca = 2.1 * 10^{-3}$ respectively. The green lines represent the Voronoi cell edges. The red line segment represents the growing edge shared by a pair of converging drops during the T1 events. The blue dots represent the centers of 5-edged Voronoi cells. (c)-(e) Length of the growing edges as a function of time for: (c) $10^{-7} < Ca < 10^{-6}$, (d) $10^{-6} < Ca < 10^{-3}$, and (e) $10^{-3} < Ca < 10^{-2}$. Each set of symbols represents the measurement of one T1 event at a given *Ca*.

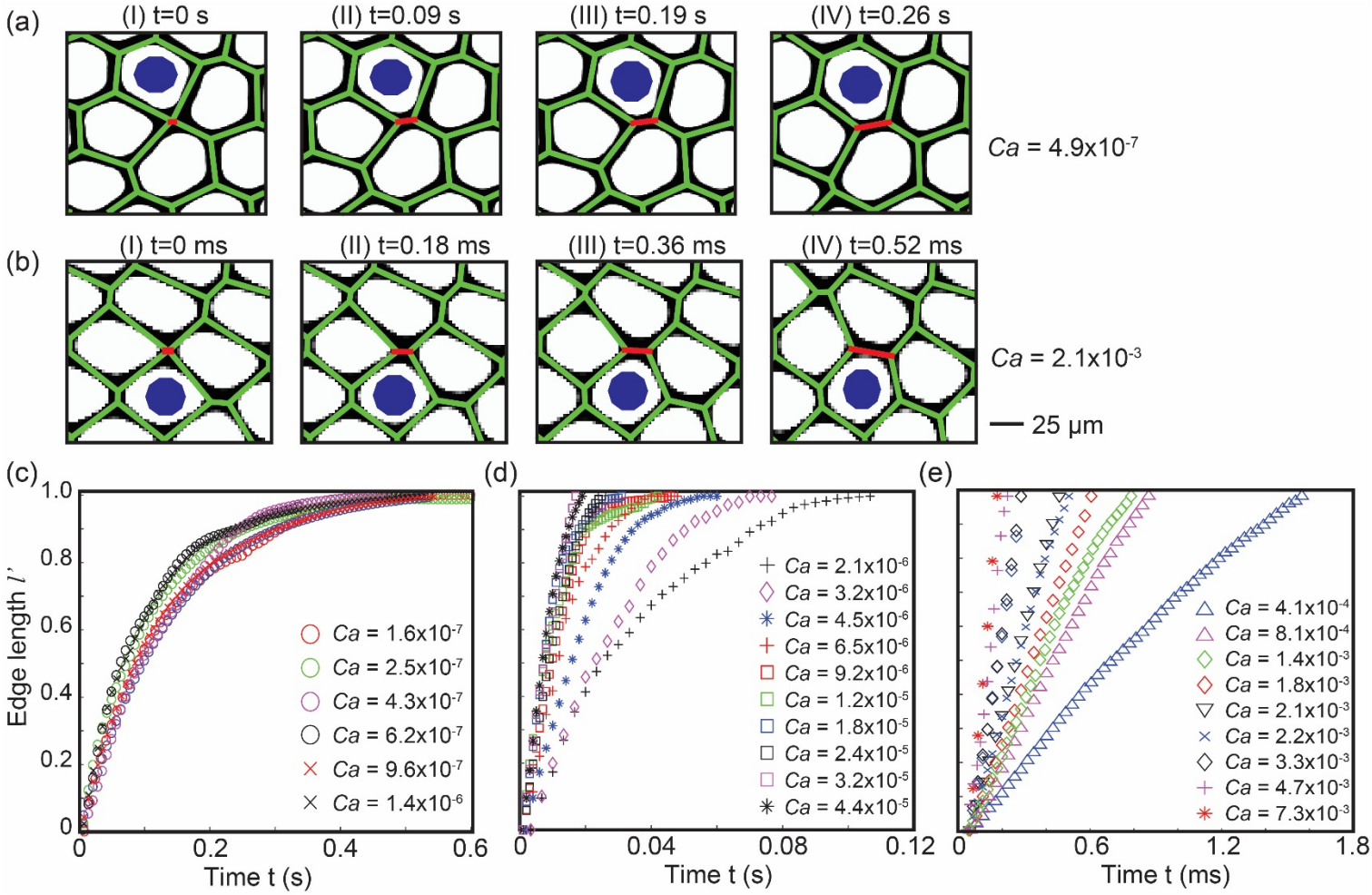

Figure 3. (a) Representative distribution of dimensionless T1 duration $T'/\langle T'\rangle$at various *Ca*. Each distribution consists of a batch of *T'* measurements of >200 T1 events within one CV at a given flow rate *Q*. *T'* was normalized by $\langle T'\rangle$, the value of *T'* averaged over >200 measurements. The dashed line is a visual guide only. (b) Log-log plot showing *T'* as a function of *Ca*. Each data point consists of a batch of *T'* measurements of >200 T1 events within one CV at a given flow rate *Q*. The vertical and the horzontal error bars represent the standard deviation in *T'* and that in *Ca* for all >200 measurements within one CV at one value of *Q*, respectively (see section 2.6). The three dashed lines have logarithmic slopes of -0.14, -0.61, and -0.37, respectively.

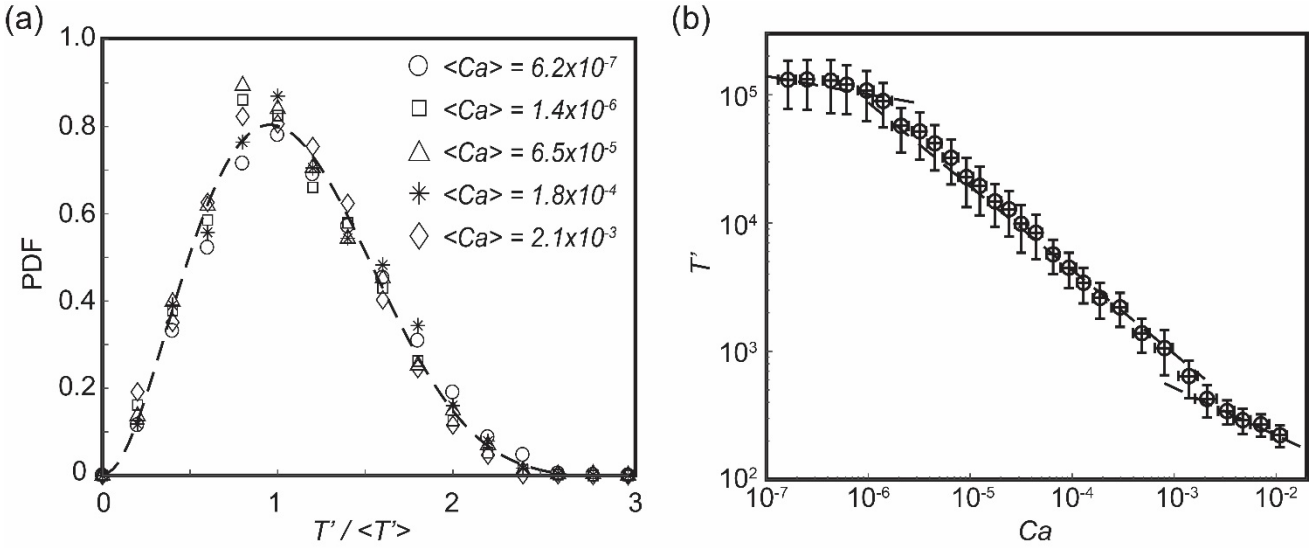

Figure 4. (a) Scaled T1 event count P_{T1} as a function of *Ca*. (b) Time between two successive T1 events *dT'* as a function of *Ca* in a log scale. The results of $\langle T' \rangle$ in Figure 3b are also shown for a direct comparison. The dashed line shows a fit to the *dT'* data. It has a logarithmic slope of -0.86. (c)-(e) Distribution of event onset time t_{T1} normalized by $\langle T \rangle$ at: (c) $\langle Ca \rangle = 2.5 \times 10^{-7}$, (d) $\langle Ca \rangle = 2.4 \times 10^{-5}$, and (e) $\langle Ca \rangle = 1.4 \times 10^{-3}$, respectively.

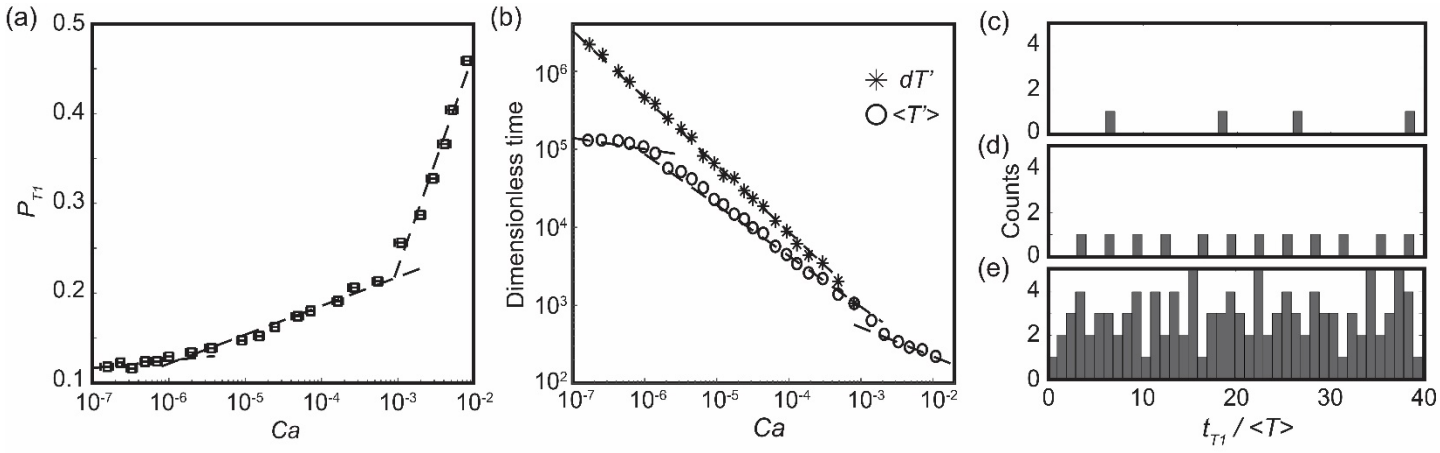

Figure 5 (a)-(c) Spatial distribution of T1 events for *Ca* ranges of (a) $1.1 \times 10^{-7} < Ca < 1.6 \times 10^{-6}$ (within Regime 1), (b) $8.5 \times 10^{-6} < Ca < 6.3 \times 10^{-5}$ (within Regime 2), and (c) $7.9 \times 10^{-4} < Ca < 8.5 \times 10^{-3}$ (within Regime 3), respectively. The *Ca* range is measured from the left edge ($x = 0$) to the right edge ($x = x_{max}$) of the channel. To obtain the spatial distribution, we generated 10 μm-by-10 μm mesh grids in the field of view and counted the number of T1 events that occurred within each grid. The location of each marker represents the center of a grid. The color of the markers represents the number of T1 events that occurred in the corresponding grid. The white space between the markers have no recorded T1 events. Each plot was generated by tracking a total of 2000 drops advected through the field of view. The dashed box marks the boundaries of the control volume (CV).

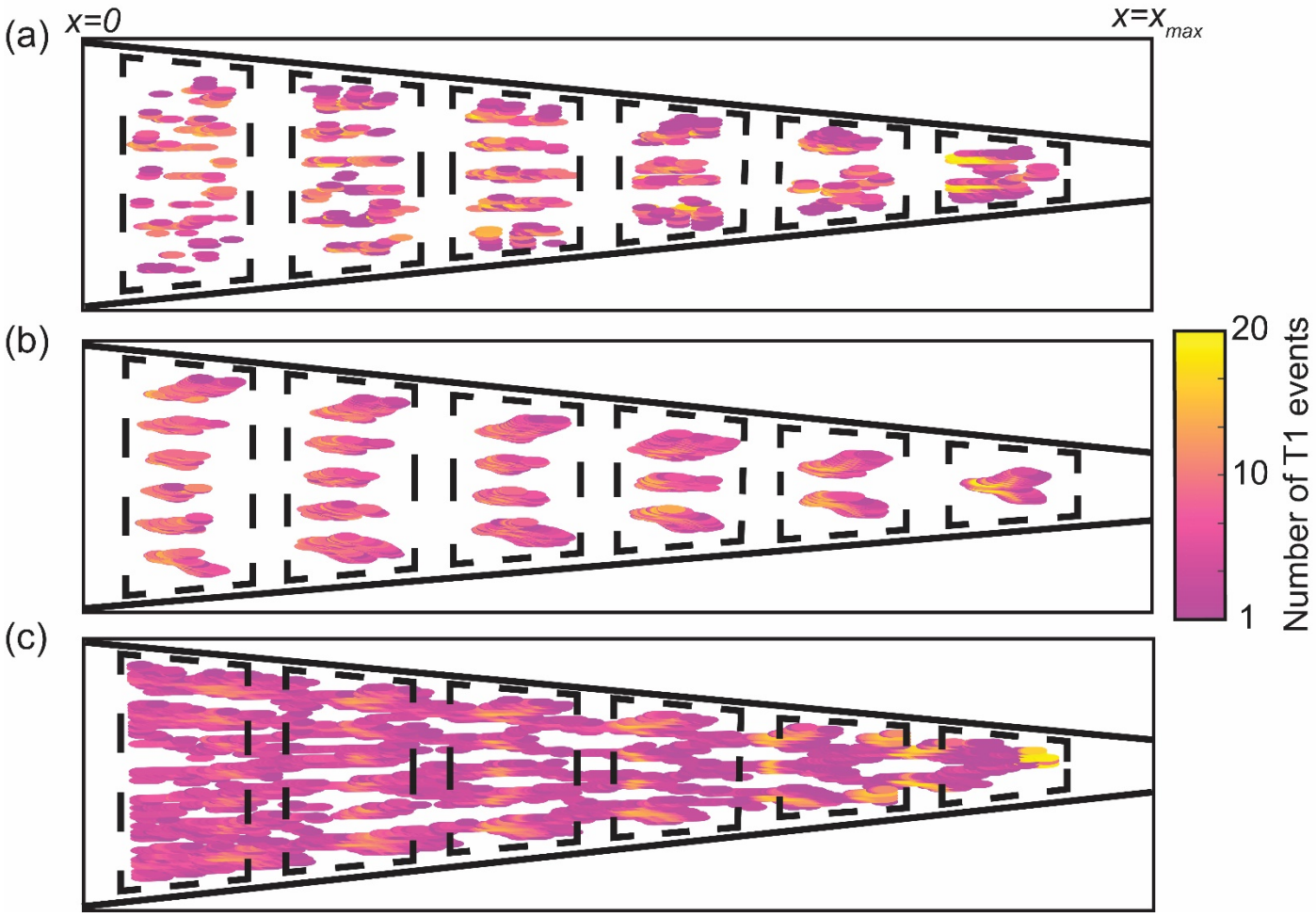

Figure 6. (a)-(c) Trajectories of 2000 droplets advected through the channel for: (a) $1.1 \times 10^{-7} < Ca < 1.6 \times 10^{-6}$ (within Regime 1), (b) $8.5 \times 10^{-6} < Ca < 6.3 \times 10^{-5}$ (within Regime 2), and (c) $7.9 \times 10^{-4} < Ca < 8.5 \times 10^{-3}$ (within Regime 3), respectively. Each marker represents the instantaneous position of the centroid of one droplet. The insets are time-averaged, x-component of droplet velocity ($\overline{U_x}$) across the width of the channel calculated at the locations marked by the red and green boxes, respectively. $\overline{U_x}$ is normalized to $\overline{U_{x_{max}}}$, the maximum x-component of velocity observed in the constriction. The rearrangement zones are indicated by blue arrows in (a) and (b). **(d)-(f)** Snapshots of successive T1 events at: (a) $\langle Ca \rangle = 2.5 \times 10^{-7}$ (Regime 1), (b) $\langle Ca \rangle = 1.2 \times 10^{-5}$ (Regime 2), and (c) $\langle Ca \rangle = 1.4 \times 10^{-3}$ (Regime 3), respectively. The blue arrows indictae the direction along which successive T1 events occur. For T1 events along the 60 degree slip plane, the converging (diverging) drops are colored in green (red). For T1 events along the direction of imposed flow, the converging (diverging) drops are colored in yellow (purple). For both (d) and (e), each sequence shows 5 successive T1 events along the slip plane. For (f), the sequence shows 5 successive T1 events along the slip plane and the flow direction, respectively.

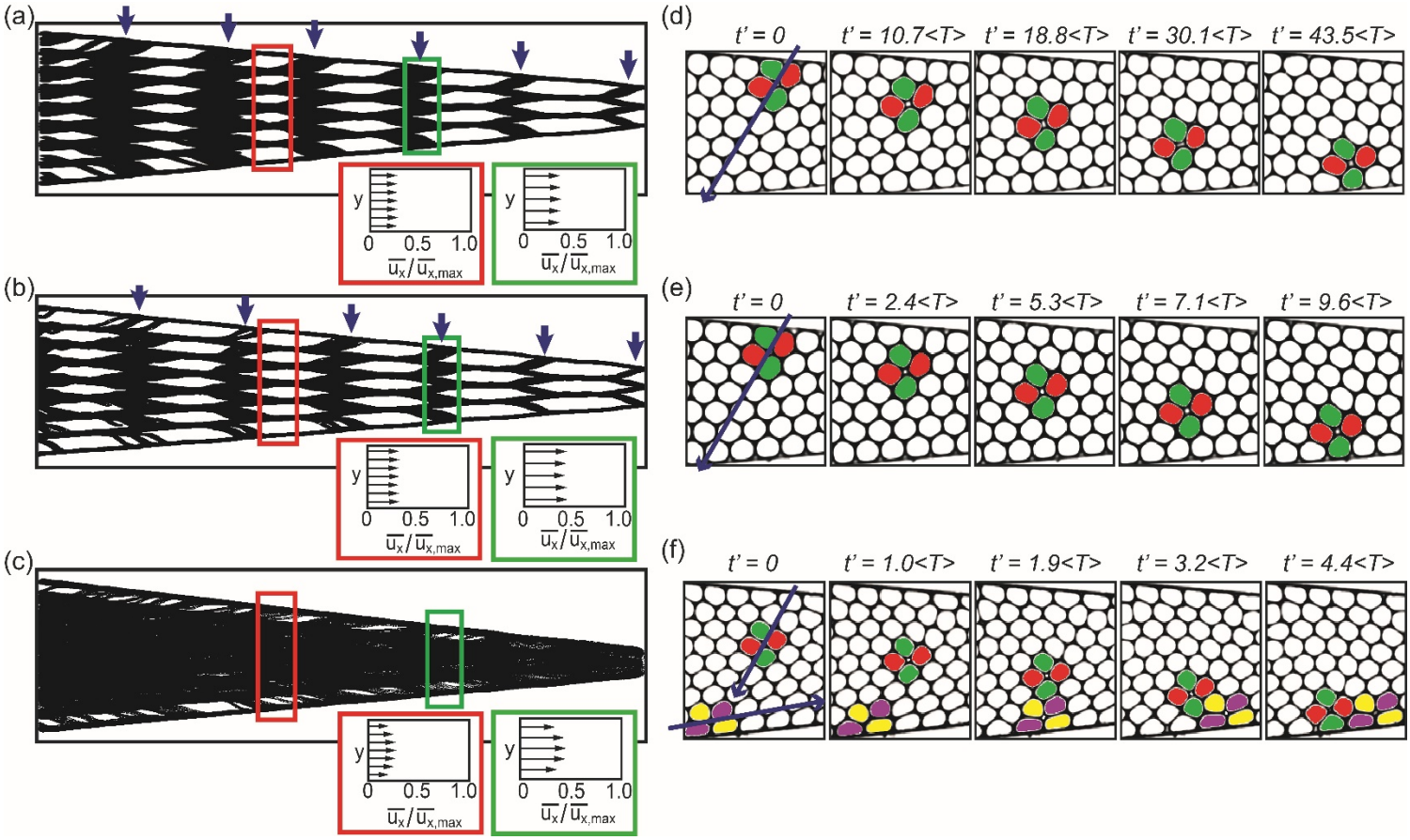

Figure 7. *dT'*, *T'*, and *De* as a function of *Ca*. $Ca_{1\text{-}2}$, $Ca_{1\text{-}2}$, and $Ca_{S\text{-}L}$ represent the transition between Regime 1 and 2, the transition between Regime 2 and 3, and the solid-like to liquid-like transition when *De* = 1, respectively.

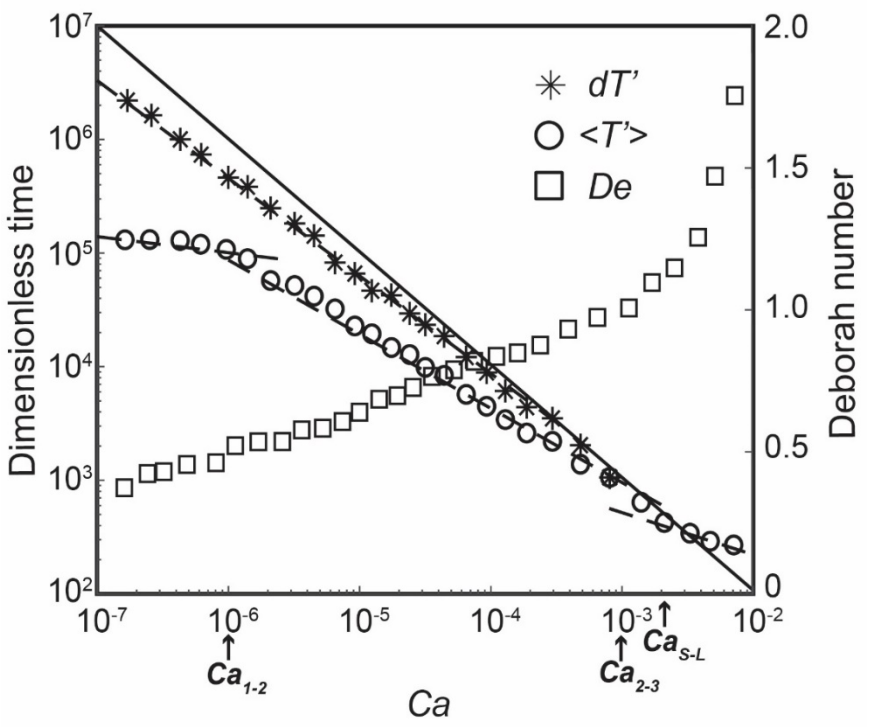

Reference

[1] I. Prigogine and I. Stengers, *Order out of chaos: Man's new dialogue with nature* (Bantam books New York, 1984), Vol. 13.
[2] A. M. Zhabotinsky, A history of chemical oscillations and waves, Chaos **1**, 379 (1991).
[3] J. K. Parrish and L. Edelstein-Keshet, Complexity, pattern, and evolutionary trade-offs in animal aggregation, Science **284**, 99 (1999).
[4] T. Thorsen, R. W. Roberts, F. H. Arnold, and S. R. Quake, Dynamic pattern formation in a vesicle-generating microfluidic device, Phys. Rev. Lett. **86**, 4163 (2001).
[5] P. Garstecki, M. J. Fuerstman, and G. M. Whitesides, Oscillations with uniquely long periods in a microfluidic bubble generator, Nat. Phys. **1**, 168 (2005).
[6] P. Garstecki and G. M. Whitesides, Flowing crystals: nonequilibrium structure of foam, Phys. Rev. Lett. **97**, 024503 (2006).
[7] T. Beatus, T. Tlusty, and R. Bar-Ziv, Phonons in a one-dimensional microfluidic crystal, Nat. Phys. **2**, 743 (2006).
[8] I. Shani, T. Beatus, R. H. Bar-Ziv, and T. Tlusty, Long-range orientational order in two-dimensional microfluidic dipoles, Nat. Phys. **10**, 140 (2014).
[9] Y. Gai, C. M. Leong, W. Cai, and S. K. Tang, Spatiotemporal periodicity of dislocation dynamics in a two-dimensional microfluidic crystal flowing in a tapered channel, Proc. Natl. Acad. Sci. USA **113**, 12082 (2016).
[10] H. Princen, Rheology of foams and highly concentrated emulsions: I. Elastic properties and yield stress of a cylindrical model system, J. Colloid Interface Sci. **91**, 160 (1983).
[11] L. Bécu, S. Manneville, and A. Colin, Yielding and flow in adhesive and nonadhesive concentrated emulsions, Phys. Rev. Lett. **96**, 138302 (2006).
[12] S. L. Kokal, Crude oil emulsions: A state-of-the-art review, SPE Prod. Facil. **20**, 5 (2005).
[13] M. T. Guo, A. Rotem, J. A. Heyman, and D. A. Weitz, Droplet microfluidics for high-throughput biological assays, Lab Chip **12**, 2146 (2012).
[14] J. J. Agresti *et al.*, Ultrahigh-throughput screening in drop-based microfluidics for directed evolution, Proc. Natl. Acad. Sci. USA **107**, 4004 (2010).
[15] P. Mary, A. R. Abate, J. J. Agresti, and D. A. Weitz, Controlling droplet incubation using close-packed plug flow, Biomicrofluidics **5**, 024101 (2011).
[16] L. Frenz, K. Blank, E. Brouzes, and A. D. Griffiths, Reliable microfluidic on-chip incubation of droplets in delay-lines, Lab Chip **9**, 1344 (2009).
[17] A. R. Abate, T. Hung, P. Mary, J. J. Agresti, and D. A. Weitz, High-throughput injection with microfluidics using picoinjectors, Proc. Natl. Acad. Sci. USA **107**, 19163 (2010).
[18] A. Aharoni, G. Amitai, K. Bernath, S. Magdassi, and D. S. Tawfik, High-throughput screening of enzyme libraries: thiolactonases evolved by fluorescence-activated sorting of single cells in emulsion compartments, Chem. Biol. **12**, 1281 (2005).
[19] Y. Gai, J. W. Khor, and S. K. Y. Tang, Confinement and viscosity ratio effect on droplet break-up in a concentrated emulsion flowing through a narrow constriction, Lab Chip **16**, 3058 (2016).

[20] L. Rosenfeld, L. Fan, Y. Chen, R. Swoboda, and S. K. Tang, Break-up of droplets in a concentrated emulsion flowing through a narrow constriction, Soft Matter **10**, 421 (2014).
[21] L. Rosenfeld, T. Lin, R. Derda, and S. K. Tang, Review and analysis of performance metrics of droplet microfluidics systems, Microfluid Nanofluidics **16**, 921 (2014).
[22] Y. Gai, M. Kim, M. Pan, and S. K. Tang, Amphiphilic nanoparticles suppress droplet break-up in a concentrated emulsion flowing through a narrow constriction, Biomicrofluidics **11**, 034117 (2017).
[23] T. Mason, J. Bibette, and D. Weitz, Yielding and flow of monodisperse emulsions, J. Colloid Interface Sci. **179**, 439 (1996).
[24] H. A. Barnes, Rheology of emulsions - a review, Colloids Surf., A **91**, 89 (1994).
[25] D. Chen, K. W. Desmond, and E. R. Weeks, Experimental observation of local rearrangements in dense quasi-two-dimensional emulsion flow, Phys. Rev. E **91**, 062306 (2015).
[26] D. Chen, K. W. Desmond, and E. R. Weeks, Topological rearrangements and stress fluctuations in quasi-two-dimensional hopper flow of emulsions, Soft Matter **8**, 10486 (2012).
[27] B. Dollet, A. Scagliarini, and M. Sbragaglia, Two-dimensional plastic flow of foams and emulsions in a channel: experiments and lattice Boltzmann simulations, J. Fluid Mech. **766**, 556 (2015).
[28] S. Tewari, D. Schiemann, D. J. Durian, C. M. Knobler, S. A. Langer, and A. J. Liu, Statistics of shear-induced rearrangements in a two-dimensional model foam, Phys. Rev. E **60**, 4385 (1999).
[29] K. W. Desmond and E. R. Weeks, Measurement of stress redistribution in flowing emulsions, Phys. Rev. Lett. **115**, 098302 (2015).
[30] M. Durand and H. A. Stone, Relaxation time of the topological T 1 process in a two-dimensional foam, Phys. Rev. Lett. **97**, 226101 (2006).
[31] A.-L. Biance, S. Cohen-Addad, and R. Höhler, Topological transition dynamics in a strained bubble cluster, Soft Matter **5**, 4672 (2009).
[32] C. Cassar, M. Nicolas, and O. Pouliquen, Submarine granular flows down inclined planes, Phys. Fluids **17**, 103301 (2005).
[33] R. Lespiat, S. Cohen-Addad, and R. Höhler, Jamming and flow of random-close-packed spherical bubbles: An analogy with granular materials, Phys. Rev. Lett. **106**, 148302 (2011).
[34] E. Lerner, G. Düring, and M. Wyart, A unified framework for non-Brownian suspension flows and soft amorphous solids, Proc. Natl. Acad. Sci. USA **109**, 4798 (2012).
[35] M. Dennin, Statistics of bubble rearrangements in a slowly sheared two-dimensional foam, Phys. Rev. E **70**, 041406 (2004).
[36] A. Kabla and G. Debrégeas, Local stress relaxation and shear banding in a dry foam under shear, Phys. Rev. Lett. **90**, 258303 (2003).
[37] D. A. Sessoms, H. Bissig, A. Duri, L. Cipelletti, and V. Trappe, Unexpected spatial distribution of bubble rearrangements in coarsening foams, Soft Matter **6**, 3030 (2010).

[38] B. Dollet and C. Bocher, Flow of foam through a convergent channel, The European Physical Journal E **38**, 123 (2015).
[39] Y. N. Xia and G. M. Whitesides, Soft lithography, Annu. Rev. Mater. Sci. **28**, 153 (1998).
[40] S. L. Anna, N. Bontoux, and H. A. Stone, Formation of dispersions using "flow focusing" in microchannels, App. Phys. Lett. **82**, 364 (2003).
[41] See Supplemental Material at [URL will be inserted by publisher] for the capillary number of each control volume and the details of the scaling analysis.
[42] W. Shinoda and S. Okazaki, A Voronoi analysis of lipid area fluctuation in a bilayer, J. Chem. Phys. **109**, 1517 (1998).
[43] E. A. Lazar, J. Han, and D. J. Srolovitz, Topological framework for local structure analysis in condensed matter, Proc. Natl. Acad. Sci. USA **112**, E5769 (2015).
[44] Y. Tagawa, J. M. Mercado, V. N. Prakash, E. Calzavarini, C. Sun, and D. Lohse, Three-dimensional Lagrangian Voronoï analysis for clustering of particles and bubbles in turbulence, J. Fluid Mech. **693**, 201 (2012).
[45] M. Le Merrer, S. Cohen-Addad, and R. Höhler, Bubble rearrangement duration in foams near the jamming point, Phys. Rev. Lett. **108**, 188301 (2012).
[46] H. A. Stone, Dynamics of drop deformation and breakup in viscous fluids, Annu. Rev. Fluid Mech. **26**, 65 (1994).
[47] B. P. Tighe, Relaxations and rheology near jamming, Phys. Rev. Lett. **107**, 158303 (2011).
[48] J. Brujić, C. Song, P. Wang, C. Briscoe, G. Marty, and H. A. Makse, Measuring the coordination number and entropy of a 3d jammed emulsion packing by confocal microscopy, Phys. Rev. Lett. **98**, 248001 (2007).
[49] A. Gopal and D. Durian, Shear-induced “melting” of an aqueous foam, J. Colloid Interface Sci. **213**, 169 (1999).
[50] J. R. Seth, L. Mohan, C. Locatelli-Champagne, M. Cloitre, and R. T. Bonnecaze, A micromechanical model to predict the flow of soft particle glasses, Nat. Mater. **10**, 838 (2011).
[51] K. Liu, D. Williams, and B. Briscoe, The large deformation of a single micro-elastomeric sphere, J. Phys. D **31**, 294 (1998).
[52] I. Cantat, Liquid meniscus friction on a wet plate: bubbles, lamellae, and foams, Phys. Fluids **25**, 031303 (2013).
[53] C. Raufaste, A. Foulon, and B. Dollet, Dissipation in quasi-two-dimensional flowing foams, Phys. Fluids **21**, 053102 (2009).
[54] N. Denkov, S. Tcholakova, K. Golemanov, K. Ananthpadmanabhan, and A. Lips, The role of surfactant type and bubble surface mobility in foam rheology, Soft Matter **5**, 3389 (2009).
[55] N. Denkov, S. Tcholakova, K. Golemanov, K. Ananthapadmanabhan, and A. Lips, Viscous friction in foams and concentrated emulsions under steady shear, Phys. Rev. Lett. **100**, 138301 (2008).
[56] G. Katgert, A. Latka, M. E. Möbius, and M. van Hecke, Flow in linearly sheared two-dimensional foams: From bubble to bulk scale, Phys. Rev. E **79**, 066318 (2009).
[57] S. Tcholakova, N. Denkov, K. Golemanov, K. Ananthapadmanabhan, and A. Lips, Theoretical model of viscous friction inside steadily sheared foams and concentrated emulsions, Phys. Rev. E **78**, 011405 (2008).

[58] M. Sexton, M. Möbius, and S. Hutzler, Bubble dynamics and rheology in sheared two-dimensional foams, Soft Matter **7**, 11252 (2011).
[59] J. R. Seth, C. Locatelli-Champagne, F. Monti, R. T. Bonnecaze, and M. Cloitre, How do soft particle glasses yield and flow near solid surfaces?, Soft Matter **8**, 140 (2012).
[60] S. P. Meeker, R. T. Bonnecaze, and M. Cloitre, Slip and flow in soft particle pastes, Phys. Rev. Lett. **92**, 198302 (2004).
[61] S. Cohen-Addad and R. Höhler, Rheology of foams and highly concentrated emulsions, Curr. Opin. Colloid Interface Sci. **19**, 536 (2014).
[62] D. Hull and D. J. Bacon, *Introduction to dislocations* (Elsevier, 2011), Vol. 37.
[63] M. Tsamados, Plasticity and dynamical heterogeneity in driven glassy materials, Eur. Phys. J. E **32**, 165 (2010).
[64] A. Ramachandran and L. G. Leal, The effect of interfacial slip on the rheology of a dilute emulsion of drops for small capillary numbers, J. Rheol. **56**, 1555 (2012).
[65] R. Höhler and S. Cohen-Addad, Rheology of liquid foam, J. Phys. Condens. Matter **17**, R1041 (2005).
[66] N. C. Keim and P. E. Arratia, Yielding and microstructure in a 2D jammed material under shear deformation, Soft Matter **9**, 6222 (2013).
[67] J. R. Seth, M. Cloitre, and R. T. Bonnecaze, Elastic properties of soft particle pastes, J. Rheol. **50**, 353 (2006).